**Atmospheric
Measurement
Techniques
Discussions**

Characterization of aerosol photooxidation flow reactors: heterogeneous oxidation, secondary organic aerosol formation and cloud condensation nuclei activity measurements

A. T. Lambe[1,2], A. T. Ahern[1,2], L. R. Williams[2], J. G. Slowik[3], J. P. S. Wong[3], J. P. D. Abbatt[3], W. H. Brune[4], N. L. Ng[2], D. R. Croasdale[1], J. P. Wright[1], D. R. Worsnop[2], P. Davidovits[1], and T. B. Onasch[1,2]

[1]Chemistry Department, Boston College, Chestnut Hill, MA, USA
[2]Aerodyne Research Inc., Billerica, MA, USA
[3]Department of Chemistry, University of Toronto, Toronto, ON, Canada

[4]Department of Meteorology and Atmospheric Sciences, The Pennsylvania State University, State College, PA, USA

Correspondence to: T. B. Onasch (onasch@aerodyne.com)

Characterization of aerosol photooxidation flow reactors

A. T. Lambe et al.

Title Page	
Abstract	Introduction
Conclusions	References
Tables	Figures
◄◄	►►
◄	►
Back	Close
Full Screen / Esc	
Printer-friendly Version	
Interactive Discussion	

Abstract

Motivated by the need to develop instrumental techniques for characterizing organic aerosol aging, we report on the performance of the Toronto Photo-Oxidation Tube (TPOT) and Potential Aerosol Mass (PAM) flow tube reactors under a variety of experimental conditions. The principal difference between the flow tubes was that the PAM system was designed to minimize wall effects, whereas the TPOT reactor was designed to study heterogeneous aerosol chemistry. The following studies were performed: (1) transmission efficiency measurements for CO_2, SO_2, and bis(2-ethylhexyl) sebacate (BES) particles, (2) H_2SO_4 yield measurements from the oxidation of SO_2, (3) residence time distribution (RTD) measurements for CO_2, SO_2, and BES particles, (4) chemical composition and cloud condensation nuclei (CCN) activity measurements of BES particles exposed to OH radicals, and (5) chemical composition, CCN activity, and yield measurements of secondary organic aerosol (SOA) generated from gas-phase OH oxidation of m-xylene and α-pinene. OH exposures ranged from $(2.0 \pm 1.0) \times 10^{10}$ to $(1.8 \pm 0.3) \times 10^{12}$ molec cm^{-3} s. Where applicable, data from the flow tube reactors are compared with published results from the Caltech smog chamber. The TPOT yielded narrower RTDs. However, its transmission efficiency for SO_2 was lower than that for the PAM. Transmission efficiency for BES and H_2SO_4 particles was size-dependent and was similar for the two flow tube designs. Oxidized BES particles had similar chemical composition and CCN activity at OH exposures greater than 10^{11} molec cm^{-3} s, but different CCN activity at lower OH exposures. The composition and yield of m-xylene and α-pinene SOA was strongly affected by reactor design and operating conditions, with wall interactions seemingly having the strongest influence on SOA yield. At comparable OH exposures, flow tube SOA was more oxidized than smog chamber SOA because of faster gas-phase oxidation relative to particle nucleation. SOA yields were lower in the TPOT than in the PAM, but CCN activity of flow-tube-generated SOA particles was similar. For comparable OH exposures, α-pinene SOA yields were similar in the PAM and Caltech chambers, but m-xylene SOA yields

Title Page

Abstract | Introduction

Conclusions | References

Tables | Figures

◄◄ | ►►

◄ | ►

Back | Close

Full Screen / Esc

Printer-friendly Version

Interactive Discussion

were much lower in the PAM compared to the Caltech chamber.

1 Introduction

For decades, smog chamber reactors have been used to simulate physical and chemical processes in the atmosphere (Turpin et al., 2000; Rudich et al., 2007; Kroll and Seinfeld, 2008). Such chambers range in size from $0.01\,\mathrm{m}^3$ to $250\,\mathrm{m}^3$ (Lonneman et al., 1981; Mentel et al., 1996), providing aerosol residence times of hours to days. While flow tube reactors have been used to study the chemistry of inorganic particles since the 1950s (Robbins and Cadle, 1958; Hanson and Lovejoy, 1995), their application to the study of organic surfaces (Cooper and Abbatt, 1996; de Gouw and Lovejoy, 1998; Bertram et al., 2001) and organic particles (Morris et al., 2002; Katrib et al., 2005; George et al., 2007) is relatively recent.

Flow tube reactors, with volumes typically in the range of 0.001–$0.01\,\mathrm{m}^3$, provide aerosol residence times of seconds to minutes. Despite shorter residence times, much higher oxidant concentrations are attainable, which facilitate higher exposure times equivalent to 1–2 weeks of atmospheric oxidation. Further, experiments that may take hours in a smog chamber can be performed in minutes in a flow tube, under conditions that can be better controlled with respect to oxidant concentration, contamination (Lonneman et al., 1981; Joshi et al., 1982) and wall interactions (McMurry and Rader, 1985; McMurry and Grosjean, 1985; Pierce et al., 2008). On the other hand, smog chambers with lower oxidant concentrations and longer residence times may more closely simulate atmospheric oxidation. All laboratory reactors are imperfect simulations of the atmosphere because they have walls that cause particle loss and can influence the chemistry of semivolatile organics and, thus, particle growth and composition (Matsunaga and Ziemann, 2010). Therefore, utilizing flow tubes and smog chamber reactors with different designs can complement each other, making it possible to extend studies over a range of parameters unattainable by either method individually, and ultimately lead towards a better understanding of atmospheric aerosol processes.

Title Page

Abstract | Introduction

Conclusions | References

Tables | Figures

|◄ | ►|

◄ | ►

Back | Close

Full Screen / Esc

Printer-friendly Version

Interactive Discussion

The results of laboratory aerosol experiments are used as inputs to climate models. Therefore, the evaluation of experimental uncertainties associated with measurements is needed for reliable application. The characterization of different reactor designs is important to establish the reliability of the experimental techniques.

In this paper, we compare two flow tube reactors of different designs. One is a glass flow tube of conventional dimensions (34 cm length × 7.3 cm diameter) developed at the University of Toronto for controlled heterogeneous oxidation studies of particles (George et al., 2007). The other flow tube developed at the Pennsylvania State University has a significantly larger volume (46 cm length × 22 cm diameter), providing a smaller surface-to-volume (SA/V) ratio (Kang et al., 2007). The two flow tubes are designated as the Toronto Photo-Oxidation Tube (TPOT) and Potential Aerosol Mass (PAM) reactors, respectively. An important distinction between the two flow tubes is that attempts were made to minimize wall interactions in the PAM, whereas no such attempts were made with the TPOT. The TPOT was designed to generate high OH concentrations for heterogeneous oxidation experiments. The PAM was designed for the study of gas-to-particle formation processes, and was adopted for aerosol kinetic studies by the Boston College – Aerodyne research group. The speed of flow through both flow tubes was slow: $0.35\,\mathrm{cm\,s^{-1}}$ in the TPOT and $0.37\,\mathrm{cm\,s^{-1}}$ in the PAM. The SA/V ratio is significantly smaller for the PAM ($0.23\,\mathrm{cm^{-1}}$) than for the TPOT ($2.8\,\mathrm{cm^{-1}}$); however, the larger volume of the PAM may facilitate more convection. Results are compared to smog chamber data where applicable.

The following studies were performed: (1) Transmission efficiency measurements for CO_2, SO_2, and bis(2-ethylhexyl) sebacate (BES) particles, (2) H_2SO_4 yield measurements from the oxidation of SO_2, (3) Residence time distribution (RTD) measurements for CO_2, SO_2, and BES particles, (4) Chemical composition and cloud condensation nuclei (CCN) activity measurements of BES particles exposed to OH radicals, and (5) Chemical composition, CCN activity, and yield measurements of secondary organic aerosol (SOA) generated from gas-phase OH oxidation of m-xylene and α-pinene. The purpose of the study is to assess the effects of flow tube design differences on

reactor performance and ultimately on the atmospheric relevance of laboratory-based SOA measurements.

2 Experimental

A schematic of the experimental setup is shown in Fig. 1. Gas/particle sources and monitoring instruments were shared by the TPOT and PAM, with 3-way valves placed upstream and downstream to switch flows and monitoring instruments between reactors. Input lines 1 and 2 provide gases for the production of OH radicals. Line 3 supplies gas-phase α-pinene or m-xylene for the production of SOA, or SO_2 for the production of H_2SO_4. Line 4 provides monodisperse BES particles. BES and H_2SO_4 were used as proxies for primary and secondary aerosols in specific characterization studies. Smog chamber data used in the intercomparison were obtained in the dual 28-m^3 Caltech chambers; experimental details are described in Ng et al. (2007a,b).

2.1 OH radical generation

O_3 was produced from external irradiation of O_2 with a mercury lamp ($\lambda = 185\,nm$) and was measured with an O_3 monitor (2B Technologies). Excited oxygen [$O(^1D)$] atoms are produced from UV photolysis of $O_3(\lambda = 254\,nm)$ inside the flow tubes at a relative humidity of 25–30%. The radical $O(^1D)$ then reacts with water vapor (introduced using a Nafion membrane humidifier; Perma Pure LLC) to produce OH radicals in the flow tubes. Both O_3 and OH will oxidize organic species. However, except for α-pinene experiments performed at low OH concentrations, OH was always the principal oxidant. OH exposures were obtained by measuring the decay of SO_2 due to reaction with OH at specific UV lamp intensities and O_3 concentrations. Typical OH concentrations ranged from $\sim 10^8$ to $\sim 10^{10}\,molec\,cm^{-3}$ and typical OH exposures ranged from $(2.0 \pm 1.0) \times 10^{10}$ to $(1.8 \pm 0.3) \times 10^{12}\,molec\,cm^{-3}\,s$. Assuming an average atmospheric OH concentration of $1.5 \times 10^6\,molec\,cm^{-3}$ (Mao et al., 2009), this experimental

exposure is equivalent to 0.2–14 days of atmospheric oxidation. Prior to an oxidation experiment, each flow reactor was conditioned with OH radicals until a near-zero particle background was attained.

In the Caltech chamber, OH radicals were generated by UV photolysis of H_2O_2 ($\lambda = 350$ nm). The Caltech chamber experiments typically generated $[OH] = 3.0 \times 10^6$ molec cm^{-3} for 7–11 h experimental times, covering oxidant exposures from 7.5×10^{10} to 1.2×10^{11} molec cm^{-3} s for a given experiment.

2.2 Aerosol flow reactors

2.2.1 TPOT reactor

The Toronto Photo-Oxidation Tube (TPOT) reactor combines a 1.6 L mixing chamber upstream of a 0.8 L reaction chamber and a 0.8 L bypass chamber, and is similar to the design of George et al. (2007) except that the outlet of the reaction chamber is orthogonal to the UV lamp. The glass mixing chamber is 50 cm long × 3.6 cm ID and the glass reaction chamber is 34 cm long × 7.3 cm ID. A 22.9-cm O_3-free mercury pen-ray lamp (UVP) with peak emission intensity at $\lambda = 254$ nm is mounted in the center of the reaction chamber. Carrier gas flows of 8.5 lpm N_2 and 0.5 lpm O_2 were used, with 1.6 lpm pulled through the reaction and bypass chambers and 7.4 lpm of excess flow removed prior to the mixing chamber. At these flow conditions, the average plug flow residence time (τ_{plug}; volumetric flow rate divided by reactor volume) in the TPOT mixing chamber plus the reaction chamber was 110 s. The UV lamp is surrounded by a quartz sheath tube that was continuously purged with compressed air to cool the lamp. The UV lamp material filtered out 185 nm light to prevent O_3 production. The OH exposure was varied by changing the O_3 concentration input to the mixing chamber.

2.2.2 PAM reactor

The Potential Aerosol Mass (PAM) reactor is a horizontal 15 L glass cylindrical chamber that is 46 cm long × 22 cm ID. It is different from the PAM reactor used in Kang et al. (2007), which was a vertical 19 L Teflon bag with the flow entering the top and a length of 60 cm. Carrier gas flows of 8.5 lpm N_2 and 0.5 lpm O_2 were used, with 8.5 lpm of flow pulled through the PAM and 0.5 lpm of excess flow removed prior to the reactor. At these flow conditions, the τ_{plug} was 106 s, compared to a τ_{plug} of 240 s used by Kang et al. (2007). Of the total flow, 13% is diverted at the exit through an internal perforated ring that samples air near the reactor walls to reduce wall effects. Four mercury lamps (BHK Inc.) with peak emission intensity at $\lambda = 254$ nm are mounted in teflon-coated quartz cylinders inside the chamber. The lamp-mounting cylinders were continually purged with N_2 to prevent O_3 formation and remove outgassing compounds. Unlike the TPOT and the PAM chamber in Kang et al. (2007), the OH exposure in the PAM was varied by changing the UV light intensity via stepping the lamp voltages between 0 and 110 V.

2.3 Flow tube residence time distributions

Flow tube residence time distributions (RTDs) for gas-phase species were characterized by introducing 10- and 30-s pulses of CO_2 and SO_2 into the flow tubes. CO_2 and SO_2 were used as surrogate wall-inert and wall-adhering species. Prior to SO_2 pulsed inputs, flow tube walls were passivated as much as possible by flowing SO_2 until the measured concentration was constant, at which point the flow was removed and the signal returned close to background. Pulses were obtained by opening and closing a mass-flow controller (MKS Instruments), and the CO_2 or SO_2 concentration exiting the flow tube was measured immediately downstream. Ten-second pulses of 145-nm BES particles were used to characterize RTDs for condensed-phase species. BES pulses were obtained by applying and removing voltage to a differential mobility analyzer (DMA) column, and the particle concentration exiting the flow tube was

measured with a CPC. In a separate test, we verified time definition of the 10-s pulses by transmitting the gas flow through straight copper tubing. The pulses were sharp on the timescale of the flow tube RTDs.

2.4 Particle generation

In heterogeneous oxidation experiments, BES aerosols were generated by heating liquid BES to 145 °C inside a nucleator flask. Following George et al. (2009), 145 nm BES particles were size-selected with a DMA (TSI 3071A). The DMA sheath and excess flows were balanced at 10 lpm. A 1.2 lpm monodisperse flow of BES particles was introduced into the PAM or TPOT using input line 4 (Fig. 1).

SOA was generated via gas-phase oxidation of m-xylene or α-pinene followed by homogeneous nucleation. Similarly, sulfuric acid (H_2SO_4) particles were generated by OH oxidation of SO_2. The gas-phase species were introduced into the reactor at controlled rates using a mass-flow controller. Because of greater wall interactions in the SOA formation experiments in the TPOT, higher concentrations of m-xylene and α-pinene were introduced to the TPOT (262–263 ppb) than the PAM (78–88 ppb) to achieve sufficient signal-to-noise ratio in the detection of SOA particles. Caltech chamber SOA was generated from initial m-xylene and α-pinene concentrations that ranged from 14–48 ppb (Ng et al., 2007a,b). Flow tube- and smog chamber-generated SOA was formed under low-NO_X conditions.

2.5 Particle monitoring and analysis

Immediately downstream of each flow tube, annular denuders loaded with silica gel dessicant and Carulite 200 catalyst (Carus Corp.) removed water (RH < 20%) and ozone (denuding efficiency > 80%) prior to measurements. Particle number concentrations and size distributions were measured with a TSI scanning mobility particle sizer (SMPS). Bulk chemical composition of the aerosol was measured with an Aerodyne compact and high-resolution time-of-flight aerosol mass spectrometer (c-ToF-AMS,

HR-ToF-AMS; Drewnick et al., 2005; DeCarlo et al., 2006). Elemental analysis (Aiken et al., 2008) was performed on the HR-ToF-AMS data to determine the aerosol oxygen-to-carbon (O/C) ratio, used as a proxy for the aerosol oxidation level (Kroll et al., 2009). For experiments where HR-ToF-AMS data was unavailable, we applied HR-ToF-AMS-derived calibration factors relating the O/C ratio to the fraction of organic signal at $m/z = 44$ (f_{44}) to c-ToF-AMS measurements. These calibrations are shown in Fig. A1.

CCN activity of particles was measured with a Droplet Measurement Technologies CCN Counter (Roberts and Nenes, 2005). The fraction of activated particles was determined by measuring total particle concentrations with a CPC (TSI 3022A) colocated with the CCN. A DMA upstream of the CCN and CPC was used to select a dry mobility diameter (D_m) of 145 nm for oxidized BES particles and 50 nm for m-xylene/α-pinene SOA particles. For each D_m, the CCN column temperature gradient was systematically varied between 0.1–1.5% water vapor supersaturation or until 100% activation was reached, whichever occurred first. Example CCN activation curves are shown in Fig. A2.

SOA yields were calculated from the ratio of aerosol mass formed to precursor gas reacted. The aerosol mass was calculated from the integrated particle volume and the effective particle density ($\rho = D_{va}/D_m$), where D_{va} is the mean vacuum aerodynamic diameter and D_m is the electric mobility diameter. Yields were corrected for UV lamp-induced temperature increases in the PAM by applying yield corrections of −0.02 per degree K of temperature rise (Stanier et al., 2007; Qi et al., 2010) relative to room temperature. These temperature corrections typically ranged from 10–20%. Caltech smog chamber yields were corrected for wall losses using size-dependent ammonium sulfate wall-loss measurements. The magnitude of these wall loss corrections typically ranged from 10–30%.

3 Results and discussion

3.1 Flow tube transmission efficiencies

3.1.1 Gas-phase transmission efficiencies

Pulsed inputs of CO_2 and SO_2 (10 and 30 s in duration) were used to measure the transmission efficiencies of inert (CO_2) and wall-adhering (SO_2) gases. Because SO_2 can adhere to walls, the flow tubes were passivated prior to measurements as discussed in Sect. 2.3. For each gas-phase species, transmission efficiency was measured for 7–10 pulses. The measured CO_2 transmission efficiency was 0.97 ± 0.10 for the TPOT and 0.91 ± 0.09 for the PAM (uncertainties represent $\pm 1\sigma$ in measurements unless otherwise noted). The SO_2 transmission efficiency was 0.45 ± 0.13 for the TPOT and 1.2 ± 0.4 for the PAM. Within measurement uncertainty, transmission efficiency was independent of pulse duration and approximately unity for both flow tubes with the exception of SO_2 in the TPOT. Comparing SO_2 and CO_2 transmission efficiencies suggests that SO_2 wall loss is negligible in the PAM but is significant (~55%) in the TPOT for pulsed experiments. The significant, irreversible wall loss of SO_2 in the TPOT for this study was likely due to a chemical adsorption/reaction process that was not fully passivated at the time of the experiment. If this process has a constant SO_2 uptake rate, it should not affect our interpretations of the residence time distribution measurements.

3.1.2 Particle transmission efficiency

Monodisperse BES particles were size-selected with D_m ranging from 50–300 nm to measure size-dependent particle transmission efficiencies in the flow tubes. Transmission efficiency was calculated from two CPC instruments; one at the input, the other at the output of the flow tubes, that agreed to within $\pm 5\%$ when sampling the same flow. Figure 2 shows the transmission efficiency of BES particles through the TPOT and PAM

as a function of D_m. Transmission efficiencies were similar for both instruments from $D_m > 75$ nm, though the TPOT experienced more particle loss at the smallest particle size (50 nm). Particle losses through copper tubing upstream and downstream of the flow tubes were negligible. The particle transmission efficiencies for the two systems

5　have the same size-dependent trends as simple theory predicts (Hinds, 1999); however, the magnitudes of particle losses are greater. The reason for the discrepancy may be due to (a) expansions and contractions in the flow tube designs that are not accounted for in the simple theory and may induce convection in the flow tubes, or (b) the non-conducting Pyrex material of both flow tubes may induce greater particle

10　losses due to electrostatic deposition.

3.2 H_2SO_4 yield measurements

H_2SO_4 yield measurements were chosen to evaluate the measurement of secondary aerosols yields in the flow systems. SO_2 oxidation is a relatively simple system with a single rate-limiting step in the presence of gas-phase water, has a known rate con-

15　stant, and generates a well-characterized binary component particle (H_2SO_4 and H_2O). However, it may not be a perfect surrogate for SOA because the wall loss behaviour of the product gases (i.e., H_2SO_4 and semivolatile organic compounds) may differ. The transmission efficiency for H_2SO_4 was calculated from the ratio of the measured aerosol mass to the theoretical H_2SO_4 yield from the known SO_2–OH reaction. Be-

20　cause the H_2SO_4 mass measurement includes water taken up by the H_2SO_4 particles, calculations were performed to extract the dry H_2SO_4 mass from H_2SO_4–H_2O particles as discussed in Appendix A. Higher SO_2 concentrations were used in the TPOT to compensate for larger SO_2 wall losses: 77–84 ppb in the TPOT and 10–62 ppb in the PAM.

25　Two trends were observed in both flow tubes. First, at a specific OH concentration, increasing the SO_2 concentration increased the transmission efficiency of H_2SO_4 because a smaller fraction of SO_2 was required to passivate the walls leaving more SO_2 to form H_2SO_4. Second, H_2SO_4 transmission efficiency was affected by the

OH concentration. At low OH concentration, the SO_2 lifetime was longer ($\tau \sim 140$ s) and H_2SO_4 yield was more affected by SO_2 wall loss. At high OH concentration, SO_2 was oxidized more quickly ($\tau \sim 30$ s), and H_2SO_4 yield was less affected by SO_2 wall loss. As the OH exposure was increased from about 4×10^{11} molec cm^{-3} s to

5 1.8×10^{12} molec cm^{-3} s in the TPOT, the H_2SO_4 mean volume-weighted D_m increased from 50 nm to 86 nm while the transmission efficiency increased from 0.14 to 0.44. Over a similar OH exposure range in the PAM, the mean H_2SO_4 D_m increased from 65 nm to 75 nm while the transmission efficiency increased from 0.30 to 0.51. Average H_2SO_4 transmission efficiencies in the TPOT and PAM are plotted in Fig. 2 as a func-

10 tion of mean volume-weighted mobility diameter. The particle transmission efficiencies through the flow tubes are shown to be similar for BES and H_2SO_4 particles. For the test conditions here, the yields for SO_2 oxidation (H_2SO_4 particle formation) saturate at transmission efficiencies of ∼0.5 due to size-dependent particle losses in the flow reactors. Thus, yield measurements of SO_2 oxidation in the flow tubes is a function of SO_2

15 loss to walls (until saturated) and the depositional loss of the resulting particles inside the reactors prior to detection. SOA reaction yields measured in flow tubes reactors will have similar experimental dependencies.

3.3 Flow tube residence time distributions (RTDs)

Residence time distributions (RTDs) of the two flow tube reactor designs were charac-

20 terized with an inert gas (CO_2), a wall-adhering gas (SO_2), and a low-volatility spherical particle (BES). Figure 3a and b show representative residence time distribution measurements for CO_2, SO_2 and BES pulsed inputs to the TPOT and the PAM, respectively. The pulses were produced as discussed in Sect. 2.3, with each species added individually. Figure 3c compares the measured RTDs for CO_2 in the TPOT and the PAM.

25 Three sets of observations are evident from Fig. 3.

The first observations relate to the shape and width of the RTDs measured with CO_2. Figure 3c shows measured RTDs for CO_2 in the TPOT and in the PAM plotted with theoretical RTDs for reactors with ideal plug flow and ideal laminar flow characteristics.

The theoretical RTDs were calculated assuming an average residence time of 100 s (compared with 110 and 106 s plug flow residence times for the TPOT and PAM, respectively). Under plug flow conditions, the RTD is the duration of the pulse delayed by the transit time through the flow tube. Under laminar flow conditions, the shortest transit time through the flow tube is half of the average residence time. The initial shapes of both flow tube RTDs are similar to the theoretical laminar flow predictions, though the measured RTDs occur earlier in time, and both measured RTDs exhibit tailing at longer times. To gain a fuller understanding of the flow conditions in both systems, we modelled the RTDs as a laminar flow broadened by axial and radial diffusion using a Taylor dispersion model (Taylor, 1953). A best fit to our measurements required that we assumed two flow regimes: (1) a primary component that passes through the reactors without recirculation, and (2) a secondary component that is slower and more diffuse due to convection-induced recirculation within the reactors. The flow model results are shown by the dashed black traces in Fig. 3c. The model, described in Appendix A, predicts less recirculation (i.e., smaller secondary flow component) in the TPOT than in the PAM (Fig. A3), which is in agreement with the observations that show narrower RTDs in the TPOT.

The second set of observations from Fig. 3 are that the RTDs from the SO_2 pulses are delayed relative to the CO_2 pulses. In the absence of wall interactions, the CO_2 and SO_2 RTDs are expected to be the same. Therefore, this delay indicates SO_2-wall interactions. In the TPOT, the SO_2 pulse was delayed relative to the CO_2 pulse by 40–50 s (refer to Appendix A). A delay was also observed in the PAM, but it was smaller (~20 s) due to the lower SA/V ratio. The SO_2 RTD experiments show unambiguous wall effects on gas-phase precursors in the flow tube reactor designs. How these wall effects impact chemical and yield measurements of secondary organic aerosol (SOA) will depend upon oxidation rates and accommodation coefficients of the precursor and intermediate gases by the walls.

The third set of observations are that the BES RTDs were narrower than the corresponding CO_2 and SO_2 RTDs in both flow tubes. This was likely due to either (a)

poor mixing of the particles into the carrier gas flow prior to the reactors, or (b) greater fractional particle losses for particles entrained in convection currents (i.e., longer residence times in reactors with more potential for wall interactions). For the PAM, the difference between BES particles and gas-phase species was more pronounced than in the TPOT, possibly because the mixing time upstream of the PAM was significantly shorter or because longer residence times due to recirculation of the flow resulted in higher particle losses in the PAM than in the TPOT.

The measured RTDs have several implications for accurately comparing aerosol chemistry measurements from one system to another. The measured RTDs for these flow tube systems are asymmetric in time with a sharp peak at $\leq 50\%$ of the plug flow residence time and a significant tail to times greater than τ_{plug}. Pulsed aerosol chemistry experiments with high time resolution detection techniques may provide more accurate results over a range of OH exposures than steady-state flowing experiments. Further, the wall-adhering SO_2 experiments show that the average (RTD-weighted mean) residence are times greater than that predicted from the CO_2 experiments, indicating that the OH exposure is dependent upon the precursor gas wall interactions (i.e., volatility, mass accommodation, and SA/V ratio of the system). Finally, the BES experiments suggest a similiar asymmetry in the measured RTDs and corresponding residence times in flow tube reactors for heterogeneous reaction experiments, with the added uncertainty of increasing particle losses with residence time due to recirculation.

3.4 Composition and CCN activity of oxidized BES

3.4.1 Composition (O/C ratio)

Figure 4a shows the evolution of the aerosol oxygen-to-carbon (O/C) ratio for BES particles ($D_m = 145$ nm) as a function of OH exposure. The equivalent atmospheric exposure, expressed in days at $[OH] = 1.5 \times 10^6$ molec cm^{-3}, is shown on the top axis. The measured O/C ratio of unoxidized BES was 0.04, compared with a molecular formula O/C ratio of 0.15 ($C_{26}H_{50}O_4$). As the OH exposure was increased, the measured O/C

ratio increased to 0.20 in the TPOT and the PAM. For the most part, the agreement between the two flow reactors was excellent. The highest O/C ratio was reached at a slightly lower OH exposure in the PAM (1.4×10^{12} molec cm^{-3} s) than in the TPOT (1.8×10^{12} molec cm^{-3} s). This observation is consistent with the differences in measured RTDs for the two flow reactors discussed above.

3.4.2 CCN activity

Figure 4b shows results of CCN activity studies expressed in terms of the critical supersaturation s_c (supersaturation level where 50% of particles are CCN-activated) of heterogeneously oxidized BES particles as a function of OH exposure. As expected, s_c decreased as the OH exposure and O/C ratio increased (Petters et al, 2006; Massoli et al., 2010). The s_c values for particles with O/C > 0.08 were between 0.40–0.67%. At an OH exposure of $\sim$1.4 $\times 10^{12}$ molec cm^{-3} s, the s_c values measured with the two flow tubes were within 40% of each other. However, at lower OH exposures for O/C < 0.08, the s_c values measured in the two flow tubes diverged considerably, differing by as much as 100%. Under the low oxidation levels with the large s_c discrepancies, the CCN activation curves for both systems are broad (Fig. A2). The s_c discrepancy and broad CCN activation curves can both be explained by the fact that (1) heterogeneous oxidation timescales of BES particles ($\sim$200–3000 s; George et al., 2007; Lambe et al., 2009) are slow compared to average particle residence times in the flow tubes, and (2) the RTDs for BES particles differ between the PAM and the TPOT at longer residence times (Figs. 3 and A3). Therefore, because the heterogeneous oxidation rates are slow and the PAM exhibits a longer tail in the measured BES RTD, the BES particles experience more oxidation in the PAM for essentially the same flow and average OH exposure conditions. The difference in the oxidation level of the BES particles for the low OH exposure conditions is highlighted by the CCN measurements (Fig. 4b), but is not as obvious in the O/C ratio measurements (Fig. 4a).

Characterization of aerosol photooxidation flow reactors

A. T. Lambe et al.

Title Page

Abstract	Introduction
Conclusions	References
Tables	Figures

|◄ | ►|

◄ | ►

Back | Close

Full Screen / Esc

Printer-friendly Version

Interactive Discussion

3.5 Composition, yield and CCN activity of *m*-xylene and α-pinene SOA

For SOA obtained from *m*-xylene and α-pinene, in addition to the data obtained with the TPOT and PAM, published yield data (Ng et al., 2007a,b) and unpublished AMS measurements obtained in the Caltech smog chamber were included in the compari-

5   son.

3.5.1 Composition (O/C ratio)

Figure 5 shows the O/C ratio as a function of OH exposure for *m*-xylene and α-pinene-generated SOA produced in the TPOT, PAM and Caltech smog chamber. The equivalent atmospheric photochemical age at $[OH] = 1.5 \times 10^6$ molec cm^{-3} is shown on the

10   top axis. As shown in Fig. 5a at low OH exposure ($< 10^{11}$ molec cm^{-3} s), the O/C ratio for *m*-xylene SOA generated in the flow tubes was 0.63 ± 0.03 in the TPOT and 0.60 ± 0.01 in the PAM. For the smog chamber-generated *m*-xylene SOA, the O/C ratio increased from 0.08 to 0.43 as a function of OH exposure. The higher O/C ratio in the flow tube SOA compared to the smog chamber was probably due to faster gas-phase

15   oxidation, resulting in higher levels of oxidation prior to nucleation. As the OH exposure was increased from $\sim 10^{11}$ to $\sim 10^{12}$ molec cm^{-3} s, the O/C ratio of *m*-xylene SOA increased to 0.77 ± 0.05 in the TPOT and 1.24 ± 0.07 in the PAM. Differences in the O/C ratio of *m*-xylene SOA at $\sim 10^{12}$ molec cm^{-3} s OH exposure may be related to different gas-phase residence time distributions (as discussed above) or to different organic

20   aerosol concentrations (C_{OA}). Lowering C_{OA} could decrease condensed-phase partitioning of semivolatile compounds with effective saturation concentrations (C^*; Donahue et al., 2006) similar to C_{OA}. This would enrich the aerosol in more-oxidized, lower-volatility products. For the most-oxidized *m*-xylene SOA, C_{OA} was higher in the TPOT (16–42 μg m^{-3}) than in the PAM (10 μg m^{-3}). If these *m*-xylene products had

25   similar C^*, their phase partitioning would be strongly affected by the difference in C_{OA}.

In Fig. 5b, the O/C ratio for α-pinene SOA generated in both flow tubes was 0.45 ± 0.02 at low OH exposures. Smog chamber-generated α-pinene SOA had O/C

ratios ranging from 0.20 to 0.30. At high OH exposures, the O/C ratio of α-pinene SOA increased to 0.70 ± 0.12 in the TPOT and 0.90 ± 0.05 in the PAM. Because C_{OA} for the most oxidized α-pinene SOA was similar in the TPOT ($C_{OA} = 124\,\mu g\,m^{-3}$) and PAM ($C_{OA} = 116$–$141\,\mu g\,m^{-3}$), the different O/C ratios of α-pinene SOA cannot be explained by C_{OA}. Differences in α-pinene SOA composition may be due to the different residence time distributions or to different flow tube designs. In the TPOT, the mixing tube upstream of the reactor flow tube (Fig. 1) allowed α-pinene and O_3 to mix and react prior to OH exposure, leading to the OH oxidation of different species. Upstream of the PAM, mixing time prior to OH exposure is minimized.

3.5.2 SOA yield

Figures 6 and 7 show yields of m-xylene and α-pinene SOA as a function of OH exposure and C_{OA}, respectively, for the TPOT, PAM and Caltech chamber. Flow tube SOA yields were corrected for size-dependent particle transmission efficiency measurements (Fig. 2), and smog chamber SOA yield were corrected using size-dependent $(NH_4)_2SO_4$ wall loss measurements (Sect. 2.5).

Figure 6 indicates that SOA yield was strongly affected by OH exposure. SOA yields in the TPOT were lower than in the PAM and Caltech chamber because of greater gas-phase wall losses. For comparable OH exposures ($\sim 10^{11}\,molec\,cm^{-3}\,s$), α-pinene SOA yields in the PAM (0.38 ± 0.08) and Caltech chamber (0.42 ± 0.06) agreed within 10%. These PAM chamber results are also consistent with those obtained by Kang et al. (2007). However, m-xylene SOA yields in the PAM (0.17 ± 0.07; $\sim 3 \times 10^{11}\,molec\,cm^{-3}\,s$ OH exposure) and Caltech chamber (0.37 ± 0.01; $\sim 1 \times 10^{11}\,molec\,cm^{-3}\,s$ OH exposure) were different. This indicates that yields of m-xylene SOA may be more sensitive to OH concentration, OH exposure or wall interactions. For lower and higher OH exposures, yields of PAM α-pinene SOA were different (0.26 ± 0.04 and 0.19 ± 0.03) than the maximum measured yield at $3 \times 10^{11}\,molec\,cm^{-3}\,s$ OH exposure. This was also the case for yields of PAM m-xylene

SOA, which were 0.024 ± 0.005 at lower exposures and 0.022 ± 0.003 at higher OH exposures. This decrease in PAM yields with increasing OH exposure may be due to SOA fragmentation to smaller, more volatile oxidation products, or to more rapid gas-phase oxidation suppressing aerosol growth (Kroll et al., 2009).

Figure 7 indicates that SOA yield was strongly affected by C_{OA}. Further, at a specific C_{OA}, SOA yield increased with decreasing reactor SA/V ratio from the TPOT (2.8 cm^{-1}) to the PAM (0.23 cm^{-1}) to the Caltech chamber (0.027 cm^{-1}). The most applicable comparison would use the same precursor concentrations and the same OH exposure. However, because of experimental constraints, these yield curves were generated using gas-phase precursor mixing ratios of 262–263 ppb in the TPOT, 78–88 ppb in the PAM, and 14–48 ppb in the Caltech chamber. Because SOA yield often increases with increasing precursor concentration (Odum et al., 1996; Kang et al., 2007), trends shown in Fig. 7 would have been even more pronounced if the initial precursor concentrations were similar in the TPOT, PAM and Caltech chamber.

As is evident in Figs. 6 and 7, at comparable OH exposures, the SOA composition and yield obtained with the flow tubes are different from those obtained in the smog chamber for m-xylene and to a lesser extent for α-pinene. While the disagreement in SOA yield between the PAM chamber and the Caltech chamber for m-xylene was also seen for the PAM chamber in Kang et al. (2007), the SOA yield for α-pinene is within the uncertainties of the SOA yields obtained in the Caltech and Kang et al. chambers. Oxidation rate, UV lamp intensity/wavelength, and/or wall effects may have influenced SOA yield. Faster gas-phase oxidation relative to nucleation could explain lower yields in the flow tubes than in the smog chamber. UV lamp intensity or wavelength could affect yield of oxidation products with strong UV absorption (e.g. organic peroxides; Presto et al., 2005). The flow tube and Caltech chamber UV lamps have a peak light output at $\lambda = 254$ nm and $\lambda = 350$ nm, respectively. However, if the flow tubes generate SOA that absorbs 254 nm light, the UV intensity in the TPOT would have to be higher than in the PAM to explain trends shown in Figs. 6 and 7. The UV intensity was not measured in the flow tubes. However, because OH exposures were similar in both flow

tubes using the same O_2, O_3 and H_2O inputs, wall effects seem to have the strongest influence on SOA yield. In particular, it is likely that the results are affected by wall losses of semivolatile oxidation products. More work is necessary to determine the effects of walls on semivolatile gases and particles in all chambers.

3.5.3 SOA CCN activity

Figure 8 plots s_c of flow tube m-xylene and α-pinene SOA particles ($D_m = 50$ nm) as a function of OH exposure. The TPOT and PAM measurements agreed within 25% and 18% for m-xylene and α-pinene SOA. As with oxidized BES particles, s_c decreased with increasing OH exposure and corresponding O/C ratio. For particles generated at an OH exposure of $\sim 1.5 \times 10^{12}$ molec cm^{-3} s, PAM SOA had a slightly higher O/C ratio and lower s_c than TPOT SOA. This is consistent with more highly-oxidized hydrophilic particles having higher water solubility.

3.6 Flow tube design modifications

Flow tube reactors can be used in a variety of ways to study aerosol chemistry, ranging from heterogeneous oxidation studies to CCN modification and SOA formation. Measurements presented in this paper suggest several design changes that are likely to modify aerosol flow tube performance. Replacing pyrex flow tube walls with a passivated conductive material could increase particle transmission efficiency by minimizing electrostatic losses. Using a flow tube with a smaller diameter-to-length ratio yields narrower flow tube residence time distributions, which ensures that chemicals within the reactor experience a more uniform OH exposure for heterogeneous oxidation experiments. However, decreasing the diameter-to-length ratio increases the SA/V ratio and losses of wall-adhering gases and their secondary aerosol yields. For SOA formation experiments, decreasing the flow tube SA/V ratio and manipulating the flows so that the sampled air is not influenced by the walls are important modifications.

4   Summary

This work evaluated two flow tube reactor designs (TPOT and PAM) in terms of gas and particle transmission efficiencies, residence time distributions (RTDs), and oxidized organic aerosols generated from gas- and particle-phase precursors (*m*-xylene, *α*-pinene, BES). The TPOT was developed for aerosol heterogeneous oxidation studies where uniform OH exposure is more important than minimizing wall losses. On the other hand, the PAM was developed with a separate flow to minimize wall interactions, as is important for SOA formation studies. First, transmission efficiency measurements for CO_2, SO_2, BES particles and H_2SO_4 were performed. Second, RTDs were measured for CO_2, SO_2 and BES particles. Third, chemical composition and CCN activity of BES particles exposed to OH radicals were characterized. Fourth, chemical composition and yield of *m*-xylene and *α*-pinene SOA generated in the TPOT, the PAM and the Caltech chamber were compared. CCN activity of SOA generated in the flow tubes was also characterized.

The main difference between the flow tubes was the degree to which gases and aerosols interacted with reactor wall surfaces. The TPOT yielded narrower RTDs because of its larger length-to-diameter ratio. However, its transmission efficiency for gas-phase SO_2 was lower than that for the PAM, either due to the increased accessibility of the walls within the reaction chamber or within the mixing chamber. SOA yields were also lower in the TPOT than in the PAM, which is consistent with enhanced wall loss of VOC oxidation products in the TPOT. Transmission efficiency for BES and H_2SO_4 particles was size-dependent and was similar for the two flow tube designs. The particle loss was sufficiently large that it needs to be accounted for in SOA formation studies.

Under similar oxidizing conditions, the chemical composition of BES particles processed in the flow tubes was similar. Hygroscopic properties (e.g., CCN activity) were similar at high oxidation conditions, but different at low oxidation conditions (Fig. 4). SOA composition and yields were strongly affected by reactor design and operating

conditions. At comparable OH exposures, flow tube SOA was more oxidized than smog chamber SOA (Fig. 5), perhaps arising from enhanced oxidation occurring prior to particle nucleation. We are not certain of the reasons for this difference, but we note that smog chamber studies have been largely unable to match field observations of the degree of oxygenation of ambient aerosol, and so future studies in this regard are warranted. Also, the flow tube studies were conducted without a seed aerosol present, whereas the smog chamber results employed a seed, which likely plays an important role in promoting aerosol growth (Kroll et al., 2007). Flow tube SOA yields were consistently lower than smog chamber SOA yields (Figs. 6 and 7). The CCN activity of flow tube-generated SOA particles was similar between the TPOT and PAM (Fig. 8).

Smog chambers require running long experiments and can only access OH exposures $< 1 \times 10^{11}$ molec cm^{-3} s, or about 1 day of atmospheric aging. Wall effects are always present and are typically accounted for using size-dependent wall loss corrections. Flow tubes can characterize aerosols over atmospheric aging timescales of 1–10 days, but require high oxidant concentrations and also have wall effects that can influence measurements. The paper illustrates the high degree of oxidation that can be achieved within such reactors. However, it also demonstrates that SOA yields from such reactors must be viewed with caution, given the important role that wall losses may be playing. A flow reactor that is operated with seed particles and/or a sheath flow to divert air near the walls should be able to minimize wall effects and give SOA yields that more closely represent true values. Overall, this work highlights the importance of flow tube and smog chamber comparisons to evaluate their utility as complementary tools for providing data inputs to climate models.

Appendix A

Supporting information

A1 O/C-f_{44} parameterizations

Figure A1 shows the aerosol O/C ratio determined from HR-ToF-AMS measurements plotted versus the fraction of organic signal at $m/z = 44$ (f_{44}) for m-xylene SOA, α-pinene SOA, and oxidized BES particles. The O/C ratio-f_{44} parametermization from Aiken et al. (2008) is also shown. Calibrations from Fig. A1 were applied to several c-ToF-AMS measurements presented in Figs. 4 and 5 where corresponding HR-ToF-AMS measurements were unavailable. The Aiken parameterization was applied to Caltech smog chamber data presented in Fig. 5.

A2 CCN activation curves

Figure A2 shows example CCN activation curves for oxidized BES particles, m-xylene SOA particles, and α-pinene SOA particles, with the CCN-activated fraction plotted as a function of water supersaturation. The critical supersaturation (50% activation level) was determined by fitting a sigmoid curve to the CCN activation curves. To indicate the effect of particle chemistry on CCN activity, the markers in Fig. A2 are colored by their corresponding O/C ratios. As the O/C ratio was increased via increasing OH exposure, the critical supersaturation decreased (Fig. 8).

A3 Taylor dispersion model for characterizing flow tube residence time distributions

As discussed in Sect. 3.3, flow tube residence time distributions (RTDs) were compared with RTDs for ideal reactor models (Fig. 3). An ideal plug flow reactor (PFR) has no axial mixing and all fluid elements have the same residence time. An ideal laminar

Discussion Paper | Discussion Paper | Discussion Paper | Discussion Paper

flow reactor also has no axial mixing, but is characterized by a wider RTD because of slower flow near the walls. The flow tube RTDs did not follow ideal reactor behaviour. Because the flow is laminar ($Re = 15$ in TPOT and $Re = 55$ in PAM), a model that describes axial dispersion in laminar flow (Taylor, 1953) was used to characterize the flow tube RTDs:

$$D_L \frac{\partial^2 C}{\partial Z^2} - u \frac{\partial C}{\partial Z} = \frac{\partial C}{\partial t} \tag{A1}$$

where D_L is the axial diffusion coefficient ($cm^2\,s^{-1}$), u is the flow velocity ($cm\,s^{-1}$), and C is the tracer concentration ($molec\,cm^{-3}$) at time t (s) and axial distance Z (cm). At $Z = L$ (reactor length), the reactor response to a pulsed tracer input is given by Eq. (A2) (Levenspiel and Smith, 1957; Hill Jr., 1977):

$$C(t) = \frac{C_o}{2\sqrt{\pi \left(\frac{D_L}{uL}\right)(t/t_{resid})}} e^{-\frac{[(1-(t/t_{resid})]^2}{\left(\frac{4D_L}{uL}\right)(t/t_{resid})}} \tag{A2}$$

where t_{resid} is the average residence time of the tracer, assuming constant fluid density. The D_L/uL quantity is proportional to the amount of dispersion ("effective dispersion coefficient").

Equation (A2) was fit to the TPOT SO_2 RTD as shown in Fig. A3c. SO_2-wall interactions in the TPOT create a wide SO_2 RTD that is well-described by Eq. (A2). Other RTDs (CO_2, BES, PAM SO_2) were characterized by a sharp initial pulse followed by a long tail (Fig. A3a,b and e,f), and Eq. (A2) did not provide a good fit. The fit to a Taylor dispersion model was improved by assuming that two dispersion timescales govern the flow (i.e., there are two distinct flow regimes). This assumption is likely to more closely model the complexity of the flow patterns: one direct flow path through the flow tube systems and a secondary flow path that undergoes recirculation within the flow tube. A modified Taylor dispersion model was derived to characterize both flow

components (first component with minor dispersion, second component with significant dispersion) and is shown in Eq. (A3):

$$C(t) = \frac{C_o}{2\sqrt{\pi \left(\frac{D_L}{uL}\right)_1 (t/t_{\text{resid}})_1}} e^{-\frac{[(1-(t/t_{\text{resid}})_1]^2}{\left(\frac{4D_L}{uL}\right)_1 (t/t_{\text{resid}})_1}}$$
$$+ \frac{C_o}{2\sqrt{\pi \left(\frac{D_L}{uL}\right)_2 (t/t_{\text{resid}})_2}} e^{-\frac{[(1-(t/t_{\text{resid}})_2]^2}{\left(\frac{4D_L}{uL}\right)_2 (t/t_{\text{resid}})_2}} \qquad (A3)$$

5 Equation (A3) was fit to CO_2, BES, and PAM SO_2 RTDs (Fig. A3a,b and d–f).

The flow model employed here provides a self-consistent, qualitative interpretation of the observed experimental results, including characterizing both components of the flow tube RTDs. The CO_2 RTD was narrower in the TPOT than in the PAM, especially for the secondary (in time) flow component, as indicated by the smaller effective dis-
10 persion coefficients (0.03 and 0.25 versus 0.03 and 0.30). The BES RTDs were also characterized by smaller dispersion coefficients in the TPOT (0.02 and 0.11) than in the PAM (0.04 and 0.26). These results suggest that less dispersion (i.e., convection) causes narrower RTDs in the TPOT than in the PAM, as expected, based on the flow tube geometries that were employed. However, our application of this model is not
15 rigorous as our specific cases do not appear to meet the strict criteria for Taylor dispersion (radial diffusion ≫ axial residence time). While several factors may help relax the criteria in our cases, including two apparently well-defined flow regimes (limiting effective radial dimensions) and the well-mixed conditions of the trace gas or particles, this model does not provide a complete physical interpretation of the measured RTDs.

A4   H$_2$SO$_4$ transmission efficiency calculations

The measured sulfuric acid aerosol mass is given by Eq. (A4):

$$H_2SO_{4,meas} = x_{H_2SO_4} \times V_{H_2SO_4 \cdot H_2O} \times \rho_{H_2SO_4 \cdot H_2O} \qquad (A4)$$

where $x_{H_2SO_4}$ is the mass fraction of H$_2$SO$_4$ in solution, $V_{H_2SO_4 \cdot H_2O}$ is the SMPS-measured particle volume (nm^3 cm^{-3}), and $\rho_{H_2SO_4 \cdot H_2O}$ (g cm^{-3}) is the density of the H$_2$SO$_4$-H$_2$O solution following water uptake by H$_2$SO$_4$. Values for $\rho_{H_2SO_4 \cdot H_2O}$ and $x_{H_2SO_4}$ were inferred from the relative humidity of the aerosol flow (Seinfeld and Pandis, 2006) sampled by the SMPS. The dry yield of H$_2$SO$_4$ from OH oxidation of SO$_2$ is 3.95 µg m^{-3} per ppb SO$_2$ reacted. Therefore, the H$_2$SO$_4$ transmission efficiency is given by Eq. (A5):

$$H_2SO_4 \text{ transmission efficiency} = \frac{H_2SO_{4,meas}}{3.95 \times \Delta SO_2} \qquad (A5)$$

where ΔSO_2 is the amount of SO$_2$ reacted (ppb) after turning on the flow tube UV lamps.

Title Page

Abstract | Introduction

Conclusions | References

Tables | Figures

◄ | ►

◄ | ►

Back | Close

Full Screen / Esc

Printer-friendly Version

Interactive Discussion

References

Aiken, A. C., Decarlo, P. F., Kroll, J. H., Worsnop, D. R., Huffman, J. A., Docherty, K. S., Ulbrich, I. M., Mohr, C., Kimmel, J. R., Sueper, D., Sun, Y., Zhang, Q., Trimborn, A., Northway, M., Ziemann, P. J., Canagaratna, M. R., Onasch, T. B., Alfarra, M. R., Prevot, A. S. H., Dommen, J., Duplissy, J., Metzger, A., Baltensperger, U., and Jimenez, J. L.: O/C and OM/OC ratios of primary, secondary, and ambient organic aerosols with high-resolution time-of-flight aerosol mass spectrometry, Environ. Sci. Technol., 42, 4478–4485, doi:10.1021/es703009q, 2008.

Bertram, A. K., Ivanov, A. V., Hunter, M., Molina, L. T., and Molina, M. J.: The reaction probability of OH on organic surfaces of tropospheric interest, J. Phys. Chem. A, 105, 9415–9421, 2001.

Cooper, P. L. and Abbatt, J. P. D.: Heterogeneous interactions of OH and HO_2 radicals with surfaces characteristic of atmospheric particulate matter, J. Phys. Chem., 100, 2249–2254, 1996.

de Gouw, J. A. and Lovejoy, E. R.: Reactive uptake of ozone by liquid organic compounds, Geophys. Res. Lett., 25, 931–934, 1998.

DeCarlo, P. F., Kimmel, J. R., Trimborn, A., Northway, M. J., Jayne, J. T., Aiken, A. C., Gonin, M., Fuhrer, K., Horvath, T., Docherty, K. S., Worsnop, D. R., and Jimenez, J. L.: Field-deployable, high-resolution, time-of-flight aerosol mass spectrometer, Anal. Chem., 78, 8281–8289, doi:10.1021/ac061249n, 2006.

Donahue, N. M., Robinson, A. L., Stanier, C. O., and Pandis, S. N.: Coupled partitioning, dilution, and chemical aging of semivolatile organics, Environ. Sci. Technol., 40, 2635–2643, 2006.

Drewnick, F., Hings, S. S., DeCarlo, P., Jayne, J. T., Gonin, M., Fuhrer, K., Weimer, S., Jimenez, J. L., Demerjian, K. L., Borrmann, S., and Worsnop, D. R.: A new time-of-flight aerosol mass spectrometer (ToF-AMS) – instrument description and first field deployment, Aerosol Sci. Tech., 39, 637–658, doi:10.1080/02786820500182040, 2005.

George, I. J., Vlasenko, A., Slowik, J. G., Broekhuizen, K., and Abbatt, J. P. D.: Heterogeneous oxidation of saturated organic aerosols by hydroxyl radicals: uptake kinetics, condensed-phase products, and particle size change, Atmos. Chem. Phys., 7, 4187–4201, doi:10.5194/acp-7-4187-2007, 2007.

George, I. J., Chang, R. Y. W., Danov, V., Vlasenko, A., and Abbatt, J. P. D.: Modification of cloud condensation nucleus activity of organic aerosols by hydroxyl radical heterogeneous

Characterization of aerosol photooxidation flow reactors

A. T. Lambe et al.

Title Page

Abstract | Introduction

Conclusions | References

Tables | Figures

|◄ | ►|

◄ | ►

Back | Close

Full Screen / Esc

Printer-friendly Version

Interactive Discussion

oxidation, Atmos. Environ., 43, 5038–5045, doi:10.1016/j.atmosenv.2009.06.043, 2009.

Hanson, D. R. and Lovejoy, E. R.: The reaction of $ClONO_2$ with submicrometer sulfuric-acid aerosol, Science, 267, 1326–1328, 1995.

Hill Jr., C. G.: An Introduction to Chemical Engineering Kinetics and Reactor Design, John Wiley and Sons, New York, 1977.

Hinds, W. C.: Aerosol Technology: Properties, Behavior, and Measurement of Airborne Particles, Wiley-Interscience, New York, 1999.

Joshi, S. B., Dodge, M. C., and Bufalini, J. J.: Reactivities of selected organic-compounds and contamination effects, Atmos. Environ., 16, 1301–1310, 1982.

Kang, E., Root, M. J., Toohey, D. W., and Brune, W. H.: Introducing the concept of Potential Aerosol Mass (PAM), Atmos. Chem. Phys., 7, 5727–5744, doi:10.5194/acp-7-5727-2007, 2007.

Katrib, Y., Bishos, G., Buseck, P. R., Davidovits, P., Jayne, J. T., Mochida, M., Wise, M. E., Worsnop, D. R., and Martin, S. T.: Ozonolysis of mixed oleic acid/stearic acid particles: reaction kinetics and chemical morphology, J. Phys. Chem. A, 109, 10910–10919, 2005.

Kroll, J. H., Chan, A. W. H., Ng, N. L., Flagan, R. C., and Seinfeld, J. H.: Reactions of semivolatile organics and their effects on secondary organic aerosol formation, Environ. Sci. Technol., 41(10), 3545–3550, 2007.

Kroll, J. H. and Seinfeld, J. H.: Chemistry of secondary organic aerosol: formation and evolution of low-volatility organics in the atmosphere, Atmos. Environ., 42, 3593–3624, doi:10.1016/j.atmosenv.2008.01.003, 2008.

Kroll, J. H., Smith, J. D., Che, D. L., Kessler, S. H., Worsnop, D. R., and Wilson, K. R.: Measurement of fragmentation and functionalization pathways in the heterogeneous oxidation of oxidized organic aerosol, Phys. Chem. Chem. Phys., 11, 8005–8014, doi:10.1039/b905289e, 2009.

Lambe, A. T., Miracolo, M. M., Hennigan, C. J., Robinson, A. L., and Donahue, N. M.: Effective rate constants and uptake coefficients for the reactions of organic molecular markers (*n*-alkanes, hopanes and steranes) in motor oil and diesel primary organic aerosols with hydroxyl radicals, Environ. Sci. Technol., 43, 23, 8794–8800, 2009.

Levenspiel, O. and Smith, W. K.: Notes on the diffusion-type model for the longitudinal mixing of fluids in flow, Chem. Eng. Sci., 6, 227–233, 1957.

Lonneman, W. A., Bufalini, J. J., Kuntz, R. L., and Meeks, S. A.: Contamination from fluorocarbon films, Environ. Sci. Technol., 15, 99–103, 1981.

Title Page

Abstract | Introduction

Conclusions | References

Tables | Figures

|◀ | ▶|

◀ | ▶

Back | Close

Full Screen / Esc

Printer-friendly Version

Interactive Discussion

Mao, J., Ren, X., Brune, W. H., Olson, J. R., Crawford, J. H., Fried, A., Huey, L. G., Cohen, R. C., Heikes, B., Singh, H. B., Blake, D. R., Sachse, G. W., Diskin, G. S., Hall, S. R., and Shetter, R. E.: Airborne measurement of OH reactivity during INTEX-B, Atmos. Chem. Phys., 9, 163–173, doi:10.5194/acp-9-163-2009, 2009.

Massoli, P., Lambe, A. T., Ahern, A. T., Williams, L. R., Ehn, M., Mikkilä, J., Canagaratna, M. R., Brune, W. H., Onasch, T. B., Jayne, J. T., Petäjä, T., Kulmala, M., Laaksonen, A., Kolb, C. E., Davidovits, P., and Worsnop, D. R.: Relationship between aerosol oxidation level and hygroscopic properties of laboratory generated secondary organic aerosol (SOA) particles, Geophys. Res. Lett., in press, doi:10.1029/2010GL045258, 2010.

Matsunaga, A. and Ziemann, P. J.: Gas-wall partitioning of organic compounds in a teflon film chamber and potential effects on reaction product and aerosol yield measurements, Aerosol Sci. Tech., 44(10), 881–892, 2010.

McMurry, P. H. and Grosjean, D.: Gas and aerosol wall losses in teflon film smog chambers, Environ. Sci. Technol., 19, 1176–1182, 1985.

McMurry, P. H. and Rader, D. J.: Aerosol wall losses in electrically charged chambers, Aerosol Sci. Tech., 4, 249–268, 1985.

Mentel, T. F., Bleilebens, D., and Wahner, A.: A study of nighttime nitrogen oxide oxidation in a large reaction chamber – the fate of NO_2, N_2O_5, HNO_3, and NO_3^- at different humidities, Atmos. Environ., 30, 4007–4020, 1996.

Morris, J. W., Davidovits, P., Jayne, J. T., Jimenez, J. L., Shi, Q., Kolb, C. E., Worsnop, D. R., Barney, W. S., and Cass, G.: Kinetics of submicron oleic acid aerosols with ozone: a novel aerosol mass spectrometric technique, Geophys. Res. Lett., 29, 1357, 2002.

Ng, N. L., Chhabra, P. S., Chan, A. W. H., Surratt, J. D., Kroll, J. H., Kwan, A. J., McCabe, D. C., Wennberg, P. O., Sorooshian, A., Murphy, S. M., Dalleska, N. F., Flagan, R. C., and Seinfeld, J. H.: Effect of NO_x level on secondary organic aerosol (SOA) formation from the photooxidation of terpenes, Atmos. Chem. Phys., 7, 5159–5174, doi:10.5194/acp-7-5159-2007, 2007a.

Ng, N. L., Kroll, J. H., Chan, A. W. H., Chhabra, P. S., Flagan, R. C., and Seinfeld, J. H.: Secondary organic aerosol formation from m-xylene, toluene, and benzene, Atmos. Chem. Phys., 7, 3909–3922, doi:10.5194/acp-7-3909-2007, 2007b.

Odum, J. R., Hoffman, T., Bowman, F., Collins, D., Flagan, R. C., and Seinfeld, J. H.: Gas/particle partitioning and secondary organic aerosol yields, Environ. Sci. Technol., 30, 2580–2585, 1996.

Title Page

Abstract | Introduction

Conclusions | References

Tables | Figures

◀ | ▶

◀ | ▶

Back | Close

Full Screen / Esc

Printer-friendly Version

Interactive Discussion

Petters, M. D., Prenni, A. J., Kreidenweis, S. M., DeMott, P. J., Matsunaga, A., Lim, Y. B., and Ziemann, P. J.: Chemical aging and the hydrophobic-to-hydrophilic conversion of carbonaceous aerosol, Geophy. Res. Lett., 33, L24806, doi:10.1029/2006gl027249, 2006.

Pierce, J. R., Engelhart, G. J., Hildebrandt, L., Weitkamp, E. A., Pathak, R. K., Donahue, N. M., Robinson, A. L., Adams, P. J., and Pandis, S. N.: Constraining particle evolution from wall losses, coagulation, and condensation-evaporation in smog-chamber experiments: optimal estimation based on size distribution measurements, Aerosol Sci. Tech., 42, 1001–1015, doi:10.1080/02786820802389251, 2008.

Presto, A. A., Hartz, K. E. H., and Donahue, N. M.: Secondary organic aerosol production from terpene ozonolysis, 1. Effect of UV radiation, Environ. Sci. Technol., 39, 7036–7045, doi:10.1021/es050174m, 2005.

Qi, L., Nakao, S., Tang, P., and Cocker III, D. R.: Temperature effect on physical and chemical properties of secondary organic aerosol from m-xylene photooxidation, Atmos. Chem. Phys., 10, 3847–3854, doi:10.5194/acp-10-3847-2010, 2010.

Robbins, R. C. and Cadle, R. D.: Kinetics of the reaction between gaseous ammonia and sulfuric acid droplets in an aerosol, J. Phys. Chem., 62, 469–471, 1958.

Roberts, G. C. and Nenes, A.: A continuous-flow streamwise thermal-gradient CCN chamber for atmospheric measurements, Aerosol Sci. Tech., 39, 206–221, 2005.

Rudich, Y., Donahue, N. M., and Mentel, T. F.: Aging of organic aerosol: bridging the gap between laboratory and field studies, Annu. Rev. Phys. Chem., 58, 321–352, 2007.

Seinfeld, J. H. and Pandis, S. N.: Atmospheric Chemistry and Physics: From Air Pollution to Climate Change, John Wiley and Sons, Inc., New York, 2006.

Stanier, C. O., Pathak, R. K., and Pandis, S. N.: Measurements of the volatility of aerosols from alpha-pinene ozonolysis, Environ. Sci. Technol., 41, 2756–2763, doi:10.1021/es0519280, 2007.

Taylor, G. I.: Dispersion of soluble matter in solvent flowing slowly through a tube, P. Roy. Soc. Lond. A, 219, 186–203, 1953.

Turpin, B. J., Saxena, P., and Andrews, E.: Measuring and simulating particulate organics in the atmosphere: problems and prospects, Atmos. Environ., 34, 2983–3013, 2000.

Title Page

Abstract | Introduction

Conclusions | References

Tables | Figures

◄◄ | ►►

◄ | ►

Back | Close

Full Screen / Esc

Printer-friendly Version

Interactive Discussion
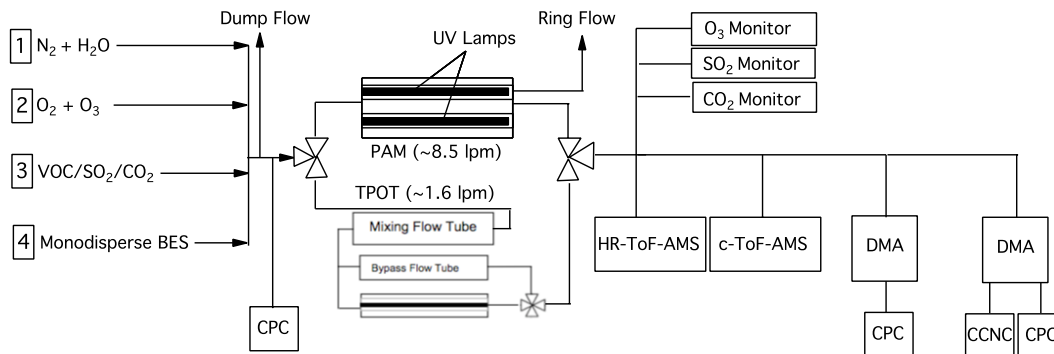
Fig. 1. Schematic of experimental setup. Gas/particle sources and monitoring instruments were shared by the PAM and TPOT flow tubes, with 3-way valves placed upstream and down-stream to switch flows and monitoring instruments between reactors. Input lines 1 and 2 provide gases for the production of OH radicals. Line 3 supplies gas-phase α-pinene or m-xylene for the production of secondary organic aerosol (SOA), or SO_2 for the production of H_2SO_4. Line 4 provides monodisperse BES particles.
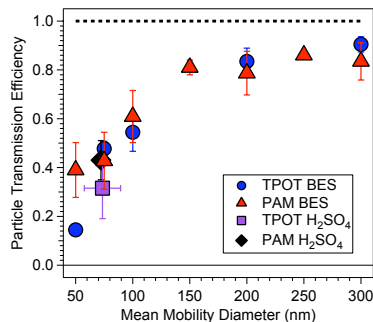
Fig. 2. Residence time distribution (RTD) measurements in the TPOT and PAM flow tubes. UV lamps were on during measurements. **(a)** CO_2, SO_2, and BES RTDs in the TPOT **(b)** CO_2, SO_2, and BES RTDs in the PAM **(c)** CO_2 RTDs in the TPOT and PAM. Theoretical plug flow and ideal laminar flow RTDs are plotted assuming an average residence time of 100 s. Dashed lines represent Taylor dispersion flow RTDs that were fit to the measurements (described in Appendix A).
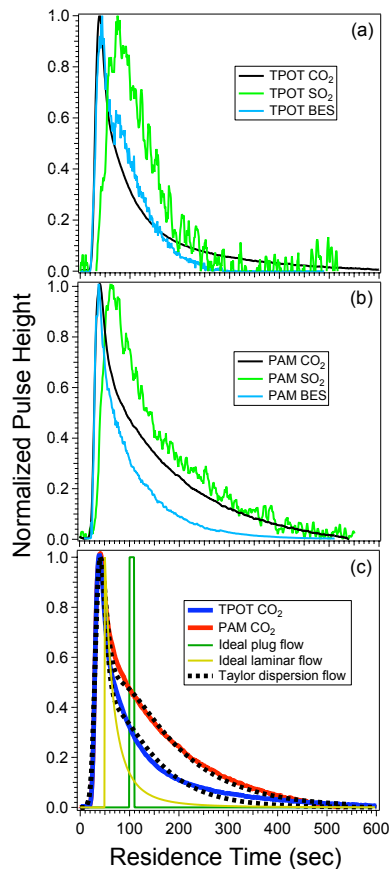
Fig. 3. Particle transmission efficiency of TPOT and PAM flow tubes as a function of mean volume-weighted mobility diameter for bis(2-ethylhexyl) sebacate (BES; circles and triangles) and sulfuric acid (H_2SO_4; square and diamond). H_2SO_4 particles were formed inside the flow tubes from SO_2 oxidation.

Title Page

Abstract | Introduction

Conclusions | References

Tables | Figures

◄ | ►

◄ | ►

Back | Close

Full Screen / Esc
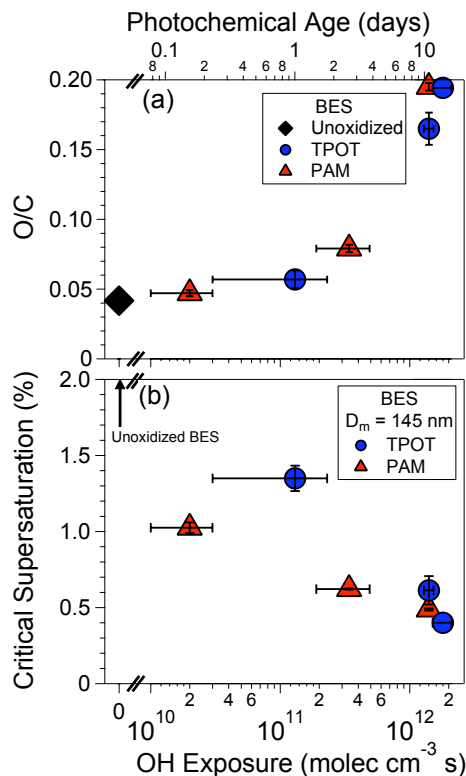
Fig. 4. (a) Aerosol oxygen-to-carbon (O/C) ratio of oxidized 145-nm BES particles as a function of OH exposure. Unoxidized BES is shown with a black diamond marker. **(b)** Critical supersaturation of oxidized BES particles ($D_m = 145$) as a function of OH exposure. Equivalent atmospheric photochemical age is shown on the top axis assuming an average OH concentration of 1.5×10^6 molec cm^{-3}. Error bars indicate calibration uncertainty in OH exposure, $\pm 1\sigma$ in O/C measurements, and $\pm 1\sigma$ in critical supersaturation measurements.

Fig. 5. Aerosol oxygen-to-carbon (O/C) ratio as a function of OH exposure for **(a)** *m*-xylene SOA and **(b)** *α*-pinene SOA in the TPOT, PAM and Caltech chamber. Markers at "zero" OH exposure indicate flow tube ozonolysis conditions with UV lamps turned off. Equivalent atmospheric photochemical age is shown on the top axis assuming an average OH concentration of 1.5×10^6 molec cm^{-3}. Error bars indicate calibration uncertainty in OH exposure, $\pm 1\sigma$ in flow tube O/C ratio measurements, and uncertainty in converting Caltech chamber $m/z = 44$ measurements to O/C ratios.
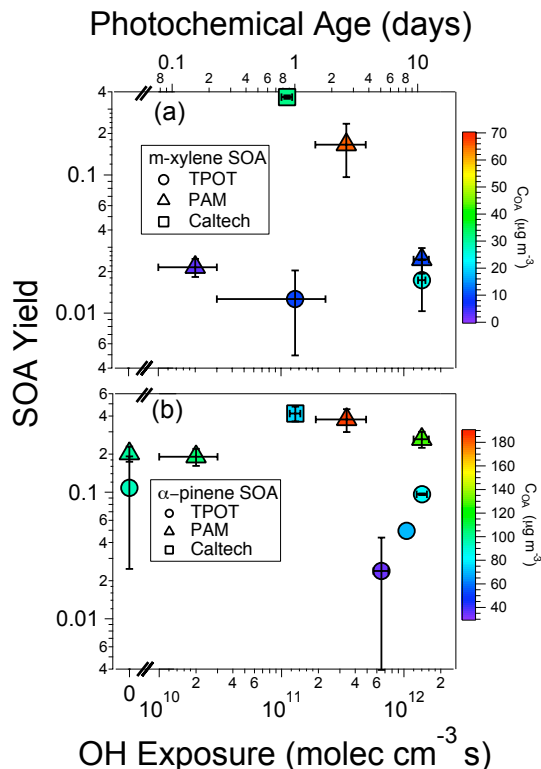
Fig. 6. SOA yield as a function of OH exposure for **(a)** *m*-xylene SOA and **(b)** *α*-pinene SOA generated in the TPOT, PAM and Caltech chamber. Markers at "zero" OH exposure indicate ozonolysis measurements with flow tube UV lamps turned off. Markers are colored by organic aerosol concentration (C_{OA}). Equivalent atmospheric photochemical age is shown on the top axis assuming an average OH concentration of 1.5×10^6 molec cm^{-3}. Error bars indicate calibration uncertainty in OH exposure and $\pm 1\sigma$ in SOA yield measurements.
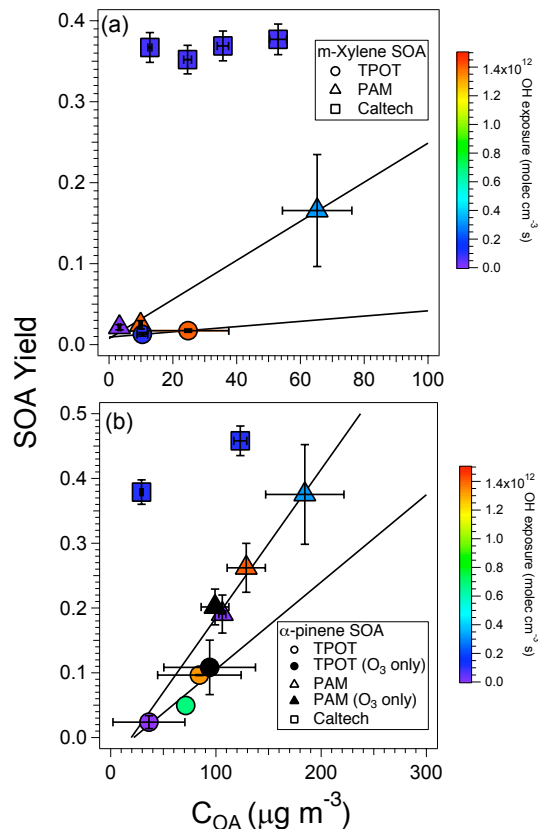
Fig. 7. SOA yield as a function of organic aerosol concentration (C_{OA}) for **(a)** m-xylene SOA and **(b)** α-pinene SOA generated in the TPOT, PAM and Caltech smog chamber. Markers are colored by OH exposure, except for black markers indicating flow tube ozonolysis conditions with UV lamps turned off. Black lines are linear fits to TPOT and PAM measurements to guide the eye. Error bars indicate $\pm 1\sigma$ in SOA yield and C_{OA} measurements.

Title Page

Abstract | Introduction

Conclusions | References

Tables | Figures

◄◄ | ►►

◄ | ►

Back | Close

Full Screen / Esc

Printer-friendly Version

Interactive Discussion
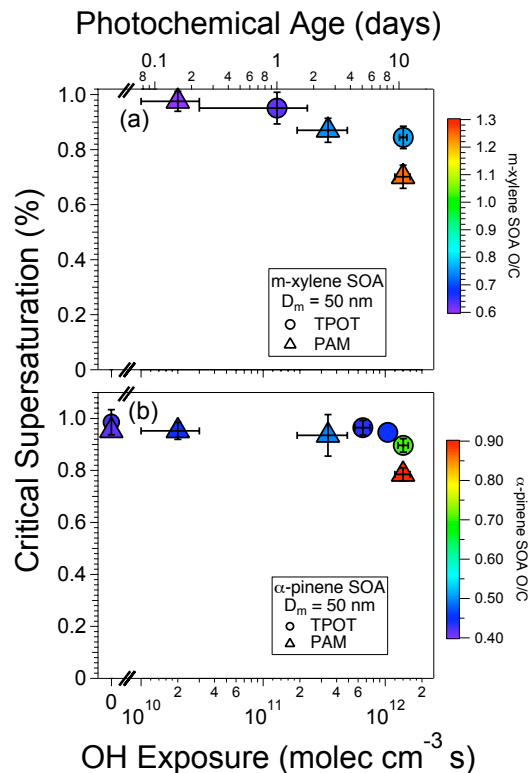
Fig. 8. Critical supersaturation of SOA particles as a function of OH exposure; data at "zero" OH exposure was generated from ozonolysis reactions with flow tube UV lamps turned off. Particles were size-selected at $D_m = 50$ nm for CCN measurements. Critical supersaturation of **(a)** m-xylene SOA particles and **(b)** α-pinene SOA particles in the TPOT and PAM are shown. Markers are colored by O/C, and equivalent atmospheric photochemical age is shown on the top axis assuming an average OH concentration of 1.5×10^6 molec cm^{-3}. Error bars indicate calibration uncertainty in OH exposure and $\pm 1\sigma$ in critical supersaturation measurements.
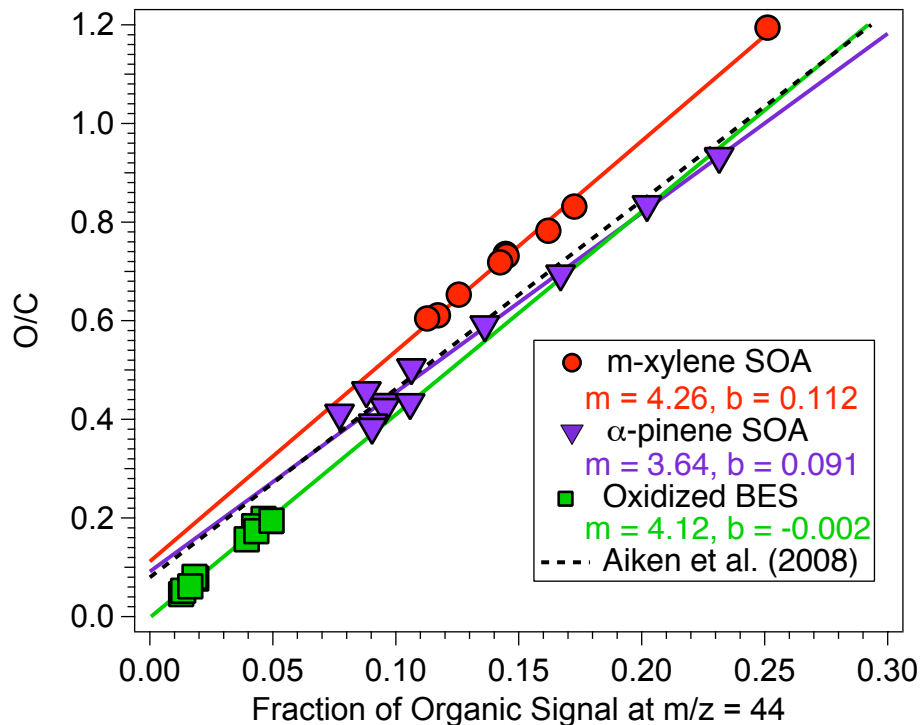
Fig. A1. Aerosol O/C ratio as a function of fraction of HR-ToF-AMS organic signal at m/z = 44 (f_{44}) for m-xylene SOA, α-pinene SOA and oxidized BES particles generated in the TPOT and PAM. Aiken et al. (2008) O/C-f_{44} parameterization is shown with a dashed line.

Title Page

Abstract | Introduction

Conclusions | References

Tables | Figures

◀ | ▶

◀ | ▶

Back | Close

Full Screen / Esc

Printer-friendly Version

Interactive Discussion
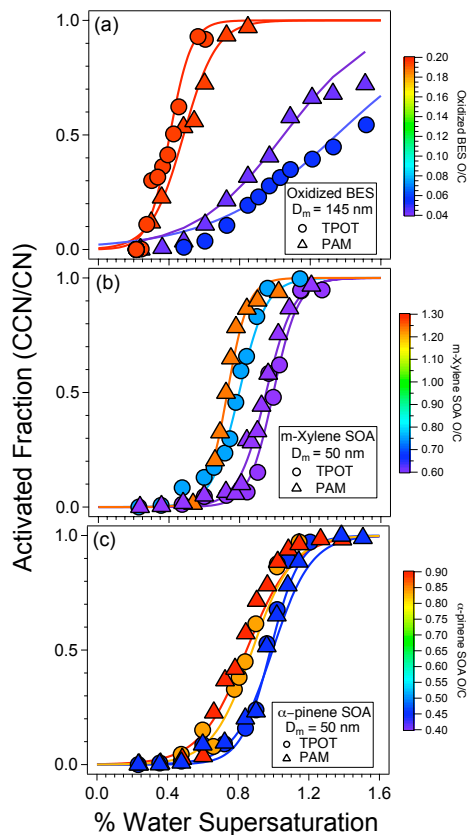
Fig. A2. CCN-activated particle fraction plotted as a function of water supersaturation for oxidized BES particles, *m*-xylene SOA particles and *α*-pinene SOA particles generated in the TPOT and the PAM. Example CCN activation curves of **(a)** 145-nm oxidized BES particles, **(b)** 50-nm *m*-xylene SOA particles, and **(c)** 50-nm *α*-pinene SOA particles are shown. Markers are colored by O/C ratio.
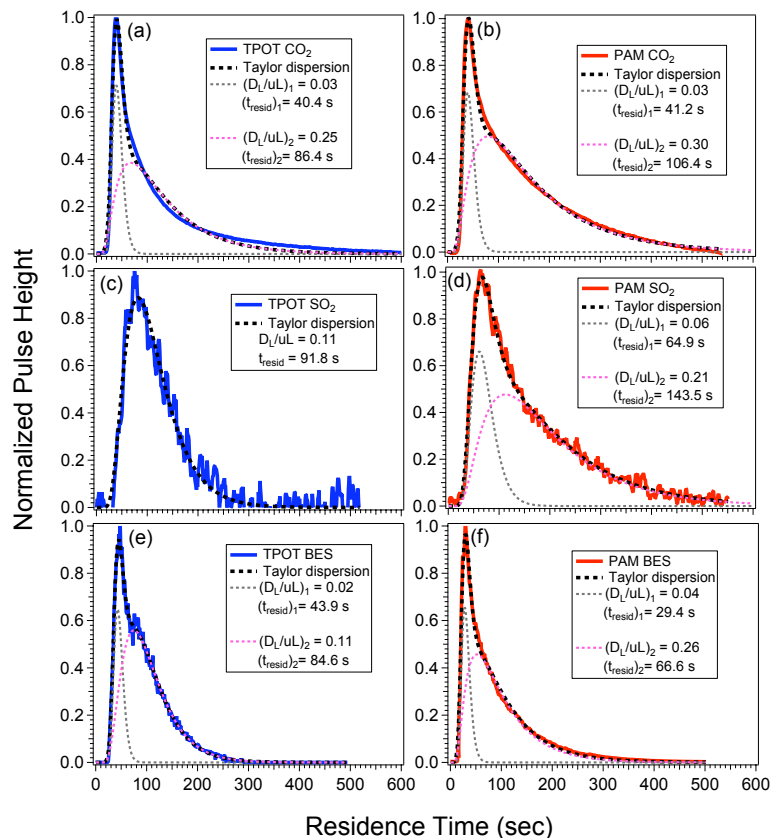
Fig. A3. Residence time distribution (RTD) measurements in the TPOT and PAM flow tubes. UV lamps were on during measurements. Measurements were fit to a Taylor dispersion model (dashed lines) with fit parameters shown in figure inserts. **(a)** CO_2 RTD in the TPOT **(b)** CO_2 RTD in the PAM **(c)** SO_2 RTD in the TPOT **(d)** SO_2 RTD in the PAM **(e)** BES RTD in the TPOT **(f)** BES RTD in the PAM.

Characterization of aerosol photooxidation flow reactors

A. T. Lambe et al.

Title Page

Abstract | Introduction

Conclusions | References

Tables | Figures

|◄ | ►|

◄ | ►

Back | Close

Full Screen / Esc

Printer-friendly Version

Interactive Discussion